Title: Temperature response of Rubisco kinetics in *Arabidopsis thaliana*: thermal breakpoints and implications for reaction mechanisms.

Running title: **Rubisco kinetic thermal breakpoints and reaction mechanisms**

Authors: Ryan A. Boyd[1,3], Amanda P. Cavanagh[2, 3], David S. Kubien[2], Asaph B. Cousins[1]*

[1]School of Biological Sciences, Molecular Plant Sciences, Washington State University, PO Box 644236, Pullman, WA 99164-4236, USA

[2]Department of Biology, University of New Brunswick, PO Box 4400, Fredericton, NB, E3B 5A3, Canada.

[3]Present address: Carl R. Woese Institute for Genomic Biology, University of Illinois at Urbana-Champaign, Urbana, IL 61801, USA

*To whom correspondence should be addressed. Email: acousins@wsu.edu

ABSTRACT

Optimization of Rubisco kinetics could improve photosynthetic efficiency, ultimatly resulting in increased crop yield. However, imprecise knowledge of the reaction mechanism and the individual rate constants limit our ability to optimize the enzyme. Membrane inlet mass spectrometery (MIMS) may offer benefits over traditional methods for determining individual rate constants of the Rubisco reaction mechanism, as it can directly monitor concentration changes in CO_2, O_2, and their isotopologs during assays. However, a direct comparsion of MIMS to the traditional Radiolabel method of determining Rubisco kinetic parameters has not been made. Here, the temperature responses of Rubisco kinetic parameters from *Arabidopsis thaliana* were measured using the Radiolabel and MIMS methods. The two methods provided comparable parameters above 25 °C, but temperature responses deviated at low temperature as MIMS derived catalytic rates of carboxylation, oxygenation, and CO_2/O_2 specificity showed thermal breakpoints. Here we discuss the variability and uncertainty surrounding breakpoints in the Rubisco temperature response and relavance of individual rate constants of the reaction mechanisms to potential breakpoints.

Keywords: Rubisco, Temperature, Kinetic breakpoints, Membrane inlet mass spectrometery, Arabidopsis, reaction mechanisms

INTRODUCTION

The enzyme Ribulose-1,5-bisphosphate carboxylase/oxygenase (Rubisco) catalyzes the reaction of CO_2 or O_2 with Ribulose-1,5-bisphosphate (RuBP) initiating the photosynthetic carbon reduction cycle or photorespiratory cycle, respectively (Bowes *et al*., 1971; Andrews *et al*., 1973). Kinetic studies on Rubisco typically report the Michaelis-Menten constants for carboxylation (K_C) and oxygenation (K_O), the catalytic rate of carboxylation (k_{catCO2}) and oxygenation (k_{catO2}), and the specificity of the enzyme for CO_2 over O_2 ($S_{C/O}$) as these parameters are used for modeling leaf gas exchange (von Caemmerer, 2000). Each of the above Michaelis-Menten parameters is a combination of elementary rate constants that describe the reaction mechanism; however, the rate constants are less well studied (Tcherkez, 2013; Tcherkez, 2016). Optimization of Rubisco kinetics for enhanced CO_2 reduction has been proposed (Spreitzer and Salvucci, 2002), but this effort is limited by our current understanding of the reaction mechanism (Tcherkez *et al*., 2006; Tcherkez, 2013).

The carboxylation and oxygenation reaction mechanisms can be separated into elementary rate constant as originally proposed by Farquhar (1979), reviewed by Tcherkez (2013) and reproduced in Figure 1. Since the initial description of the reaction mechanism (Hurwitz *et al*. 1956) there has been slow progress in defining rate constants due to experimental difficulties in isolating their individual effects. However, the use of membrane inlet mass spectrometry (MIMS) to study Rubisco kinetics may hold promise. The traditional Radiolabel method used in most Rubisco publications relies on ^{14}C assays to determine k_{catCO2}, K_C, K_O, a separate ^{3}H assay to determine $S_{C/O}$, leaving k_{catO2} to be calculated. Alternatively, the MIMS assay simultaneously measures changing concentrations of CO_2 and O_2 and can therefore determine all kinetic parameters with a single assay (Cousins *et al.*, 2010; Boyd *et al.*, 2015). An

advantage of the MIMS method is that in addition to the abundant isotopologues of CO_2 ($^{12}CO_2$) and O_2 ($^{16}O_2$) the system can monitor less abundant stable isotopologues such as $^{13}CO_2$ and $^{16}O^{18}O$. Measurements of primary kinetic isotope effects have been useful in defining enzyme reaction mechanisms (O'Leary *et al.*, 1992); therefore, the MIMS system may provide new information regarding the individual rate constants. At 25 °C the MIMS method has been used for determining both Rubisco carbon fractionation (McNevin *et al.*, 2006; McNevin *et al.*, 2007; Tcherkez *et al.*, 2013), and Michaelis-Menten constants of the carboxylation (v_c) and oxygenation (v_o) reactions (Cousins *et al.*, 2010). Additionally, it was used to determine the temperature dependencies of the Rubisco kinetic parameters in the C_4 species *Setaria viridis* (Boyd *et al.*, 2015). However, previous work using the Radiolabel method suggest lower E_a values for V_{cmax} in C_4 species than that measured by Boyd *et al*. (2015; Sharwood *et al.*, 2016; Sage, 2002; Kubien *et al.*, 2003; Perdomo *et al.*, 2015), suggesting comparisons between the MIMS E_a values and the traditional Radiolabel method are needed.

Here we measured the temperature response of Rubisco kinetic parameters from *Arabidopsis thaliana* using two methods. First, we used the traditional method involving the use of radiolabeled substrate and analysis of labeled products following the reaction in known concentrations of CO_2 and O_2 (Jordan and Ogren, 1981), which we referred to as the Radiolabel method. Secondly, we used the MIMS method following the simultaneous consumption of CO_2 and O_2 over time, giving a direct measure of v_c, v_o, CO_2, and O_2 leading to simultaneous determination of k_{catCO2}, k_{catO2}, K_C, K_O, and $S_{C/O}$ (Cousins *et al.*, 2010; Boyd *et al.*, 2015). Additionally, for the Radiolabel method we compared curve fitting CO_2 responses to determine K_C and k_{catCO2} simultaniously in an O_2 free buffer, and k_{catCO2} determined at a single bicarbonate concentration at all temperatures in open air. The later is a common practice for determining

85 k_{catCO2} temperature responses (Tieszen and Sigurdson, 1973; Sage *et al*., 1995; Crafts-Brander
86 and Salvucci, 2000; Pittermann and Sage, 2000; Sage, 2002; Kubien *et al*., 2003; Perdomo *et al*.,
87 2015).

88 Recently, the existence of breakpoints in the k_{catCO2} temperature response was highlighted
89 as a source of variability in the Rubisco temperature response literature (Sharwood *et al.*, 2016).
90 Initial observations of breakpoints in V_{cmax} temperature responses were determined to be a
91 methodological artifact due to the use of a single bicarbonate concentration at all temperatures
92 and were corrected by varying bicarbonate concentration with temperature (Björkman and
93 Pearcy, 1970). However, breakpoints were later observed for k_{catCO2}, k_{catO2}, and K_C at 15 °C using
94 a curve fitting method (Badger and Collatz, 1977). It was suggested that these breakpoints could
95 be due to changes in rate limiting steps of the reaction mechanism caused by changes in enzyme
96 conformation (Badger and Collatz, 1977). An additional breakpoint was reported in the k_{catCO2} of
97 *Oryza sativa* at 22 °C (Sage, 2002) and Kubien *et al.* (2003) observed different temperature
98 responses when k_{catCO2} was measured from 0 to 12 °C compared to 18 to 42 °C in *Flaveria*
99 *bidentis*. Most recently, Sharwood *et al.* (2016) observed breakpoints in k_{catCO2} at 25 °C for
100 Panicoid grasses when using a curve fitting method. Inconsistencies are evident between studies,
101 and it is unclear if breakpoints are universal to all temperature response studies of plant Rubisco.
102 Here, we discuss the possible causes of breakpoints, focusing on the three previously proposed
103 causes of breakpoints: erroneous bicarbonate concentrations, changes in rate limiting step of the
104 reaction mechanism, and deactivation of Rubisco at low temperature, using the Radiolabel and
105 MIMS data sets reported here.
106
107

MATERIALS AND METHODS

Plant Growth

Plants for the Radiolabel method were grown and assayed at the University of New Brunswick, Fredericton, Canada. *Arabidopsis thaliana* (Col-0) seeds were stratified for 3 days at 4 °C on Promix (Plant Products, Brampton, Canada), transferred to a growth chamber (E-15, Conviron, Winnipeg, Manitoba, Canada) and grown under photoperiod conditions of 10 h light/14 h dark, 20/18 °C, and a photosynthetic photon flux density (PPFD) of 300 µmol m^{-2} s^{-1}. Plants were watered with modified Hoagland's solution as needed.

Plants for MIMS were grown and assayed at Washington State University, Pullman, Washington, U.S.A. Seeds of *A. thaliana*, ecotype Col-0, were placed in 2 L pots containing commercial soil (LC1 Sunshine Mix, Sun Gro Horticulture, Vancouver, Canada) and grown in an environmental growth chamber (Biochambers GC-16, Winnipeg, Manitoba, Canada) at a PPFD of 300 µmol m^{-2} s^{-1} at plant height, relative humidity was not controlled, air/night temperature of 23/18 °C, with a 14 hour photoperiod and 10 hours of dark. Plants were fertilized weekly (Peters 20-20- 20, Allentown, PA, USA) and watered as needed.

Sampling for Radiolabel Analysis

Leaf punches were obtained at mid-day, flash frozen in liquid nitrogen and stored at -80 °C until extraction. Leaf tissue was ground (1.1 cm^2 disks, ca. 20 mg) in a Tenbroeck glass tissue homogenizer containing 3 mL of ice-cold extraction buffer (100 mM HEPES pH 7.6, 2 mM Na-EDTA, 5 mM $MgCl_2$, 5 mM dithiothreitol [DTT], 10 mg ml^{-1} polyvinyl polypyrolidone, 2% (vol/vol) Tween-80, 2 mM NaH_2PO_4, 12 mM amino-*n*-capronic acid, and 2 mM benzamidine)

and 50 µL Protease Inhibitor Cocktail (Sigma). This leaf homogenate was centrifuged at 16000x g at 4 °C for 60 seconds. The resulting supernatant was then desalted and concentrated as described by Cousins *et al.* (2010), and aliquots were incubated with 20 mM $MgCl_2$ and 10 mM $NaHCO_3$ at 30 °C for 20 min to fully carbamylate Rubisco. Rubisco content was quantified using [^{14}C]carboxy-arabinitol bisphosphate (^{14}CABP)-binding assay (Ruuska *et al.*, 1998, Kubien *et al.*, 2011).

Sampling for MIMS Analysis

The youngest fully expanded leaves of plants 30 to 40 days after planting were sampled for Rubisco extraction. The mid vein was removed and approximately 2 g of leaf tissue was ground in 2 mL of ice-cold extraction buffer (100 mM HEPES pH 7.8, 10 mM DTT, 25 mM $MgCl_2$, 1 mM EDTA, 10 mM NaHCO3, 1% (g/mL) PVPP, 0.5% (v/v) 100x Triton) with a mortar and pestle on ice. 67 µL of protease inhibitor cocktail (P9599, Sigma-Aldrich, St. Louis, Missouri) to 2 g of fresh leaf tissue was added to the extraction buffer before grinding. The homogenized extract was centrifuged at 4 °C, for 10 min, at 17000x g. The supernatant was collected and desalted using an Econo Pac 10DG column (Bio-Rad), filtered through a Millex GP 33-mm syringe-driven filter unit (Millipore), and then centrifuged using Amicon Ultra Ultracel 30K centrifugal filters (Millipore) at 4 °C for 1 hour at 3000x g. The layer maintained above the filter unit was collected, brought to 20% (v/v) glycerol, flash frozen in liquid nitrogen, and stored at -80 °C until measured. Rubisco content was determined as described above.

Radiolabel Measurement of Rubisco Kinetic Parameters

153 The maximum carboxylation rate of fully activated Rubisco (V_{cmax}) was measured
154 following the methods of Kubien *et al.* (2011) from 0 to 35 °C, by the incorporation of ^{14}C into
155 acid-stable products. This method is later referred to as the 'single point' method. Assays were
156 initiated by the addition of 50 µL of activated extract (as described above) to 250 µL assay buffer
157 (100 mM Bicine-NaOH (pH 8.2), 1 mM Na-EDTA, 20 mM $MgCl_2$, 5 mM DTT, 400 µM RuBP,
158 and 11 mM $NaH^{14}CO_3$ [~700 Bq $nmol^{-1}$]), and stopped after 30 to 60 seconds by adding 250 µL
159 of 1 M formic acid. Samples were dried at 90 °C, and ^{14}C acid stable products were counted
160 using a scintillation counter (LS-6500, Beckman-Coulter). Michaelis-Menten parameters for CO_2
161 (K_C), and apparent K_C at 21% O_2 ($K_{C\ (21\%\ O2)}$) were determined by assaying Rubisco activity in 7
162 mL septum-sealed, N_2-sparged vials over a range of seven $NaH^{14}CO_3$ concentrations (Paul *et al.*,
163 1991; Kubien *et al.* 2008. This analysis, referred to as the 'curve fitting' method, gave a separate
164 temperature response of k_{catCO2} from the single point method described above. Rubisco $S_{C/O}$ was
165 determined following the method described by Kane *et al.* (1994). Additional details for these
166 assays are presented in the supplemental files.
167
168 **MIMS Measurement of Rubisco Kinetic Parameters**
169 Rubisco assays were conducted in a 600 µL temperature controlled cuvette linked to an
170 isotope ratio mass spectrometer (Thermo-Fischer Delta V) and calibrated as previously described
171 (Cousins *et al.*, 2010; Boyd *et al.*, 2015). Samples were measured similar to Boyd *et al.* (2015);
172 four oxygen concentrations ranging from 40 to 1600 µM, and five CO_2 concentrations ranging
173 from 10 to 200 µM at each oxygen level were made. Measurements were made in 5 °C intervals
174 from 10 °C to 40 °C, and the same three replicates were measured at each temperature. The assay
175 buffer contained 200 mM HEPES (pH 7.7 at each measurement temperature), 20 mM $MgCl_2$, 0.1

mM α-hydroxypyridinemethanesulfonic acid (α-HPMS), 8 mg mL^{-1} CA (Sigma), and 0.6 mM RuBP. 10 µL of extract was added per measurement. Rubisco was activated by leaving the extract at room temperature for 10 minutes prior to returning to ice before measurement. Additional details for these measurements are presented in the supplemental files.

Modeling Temperature Responses

The temperature responses of the kinetic parameters were calculated for the equation

$$parameter = k_{25}\, e^{(-E_a/R\,T_K)(298.15-T_K)/(298.15)} \quad \text{Eq. 1}$$

where k_{25} is the value of the parameter at 25 °C, E_a is the Arrhenius activation energy (kJ mol^{-1}), R is the molar gas constant (0.008314 kJ mol^{-1} K^{-1}), T_K is the temperature in Kelvin, and the term (298.15-T_K)/298.15 is the scaling factor so that k_{25} may be used as the pre-exponential term. The E_a and k_{25} values for each Rubisco parameter were calculated by a linear regression of the natural log of the data plotted against (T_K-298.15)/(T_K), such that the y-intercept was equal to natural log of k_{25} and the slope was equal to E_a/(298.15 R). For comparison the non-transformed temperature response are presented in Supp. Fig. 3. Three replicates of E_a and k_{25} were determined for each parameter, with the exception of Radiolabel $S_{C/O}$ where the replication was four. For all MIMS and Radiolabel comparisons, other than $k_{catCO2,}$ only the curve fitting methods are compared. For simplicity we exclude the Radiolabel single point when comparing ratios of kinetic parameters to MIMS. Differences in the k_{25} and E_a values were determined by ANOVA, followed by pair-wise comparison (Tukey HSD) with a significance cutoff of $p < 0.05$ in Statistix 9 (Analytical Software, Tallahassee, USA).

Arrhenius plots for all kinetic parameters were examined for thermal breaks using the package 'segmented' in R, which first tests for differences between slopes using the Davies test

(Davies 1987), and then estimates the breakpoints in linear models using maximum likelihood (Muggeo 2003; Muggeo 2008; R Core Team, 2013, http://www.R-project.org/). When breakpoints in the Arrhenius temperature response plots were statistically valid, the E_a values above and below the break points were compared to other E_a values as described above, the k_{25} value was held constant when fitting for two E_a values above and below the breakpoint.

Equations for Reaction Mechanisms

Figure 1 depicts the currently hypothesized reaction mechanism of Rubisco as originally described by Farquhar (1979). The kinetic parameters k_{catCO2}, k_{catO2}, K_C, K_O, and $S_{C/O}$ can be described by the individual first order rate constants (k) seen in Figure 1 as follows:

$$k_{catCO2} = \frac{k_8 k_9}{k_8 + k_9} \quad \text{Eq. 2}$$

$$k_{catO2} = \frac{k_5 k_9}{k_5 + k_9} \quad \text{Eq. 3}$$

$$K_C = \frac{k_7 + k_8}{k_6} \frac{k_9 + k_{10}}{k_8 + k_9} \approx k_{catCO2} \frac{k_9 + k_{10}}{k_9 k_6} \quad \text{Eq. 4}$$

$$K_O = \frac{k_4 + k_5}{k_3} \frac{k_9 + k_{10}}{k_5 + k_9} \approx k_{catO2} \frac{k_9 + k_{10}}{k_9 k_3} \quad \text{Eq. 5}$$

$$S_{C/O} = \frac{k_6}{k_3} \frac{k_4 + k_5}{k_7 + k_8} \frac{k_8}{k_5} \approx \frac{k_6}{k_3}. \quad \text{Eq. 6}$$

where the subscript indicates the transition state as numbered in Figure 1 by the black circles. The approximations in Equations 4, 5, and 6 are made by assuming the rates of decarboxylation (k_7) and deoxygenation (k_4) are negligible.

These first order rate constants can be related to temperature using transition state theory and the Eyring equation

$$k = \frac{k_B T}{h} e^{-\Delta G^{\ddagger}/RT} \quad \text{Eq. 7}$$

where k_B is the Boltzmann constant ($1.3807 \cdot 10^{-23}$ J K^{-1}), h is the Planck constant ($6.6261 \cdot 10^{-34}$ J s), $\Delta G^{\ddagger}$ (J mol^{-1}) is the standard free energy difference between the transition state and the substrate (or intermediate). Note the proportionality constant κ, describing the proportion of vibrations that lead to product formation, has been assumed equal to one and left out of the equation. The $\Delta G^{\ddagger}$ has components of entropy ($\Delta S^{\ddagger}$) and enthalpy ($\Delta H^{\ddagger}$) as defined by

$$\Delta G^{\ddagger} = \Delta H^{\ddagger} - T\Delta S^{\ddagger} \qquad \text{Eq. 8}$$

where the double dagger symbol (‡) denotes the transition state.

Modeling *k* and $\Delta G^{\ddagger}$

The proposed Rubisco reaction mechanism (Fig. 1) suggests k_{catCO2}, k_{catO2}, K_C, K_O, and $S_{C/O}$ are described by complex terms made up of two or more elementrary reaction rates (Farquhar, 1979; Equations 2 through 6). The rate of an elementary reaction (k) is related to the energy barrier for the transition state of the reaction, often referred to as the activation energy ($\Delta G^{\ddagger}$). The relationship between k, $\Delta G^{\ddagger}$, and temperature is described by the Eyring equation (Equation 7), where $\Delta G^{\ddagger}$ has enthalpic ($\Delta H^{\ddagger}$) and entropic ($\Delta S^{\ddagger}$) components (Equation 8). From Equation 8, a plot of $\Delta G^{\ddagger}$ with temperature has a slope of $\Delta S^{\ddagger}$ and a y-intercept of $\Delta H^{\ddagger}$. For the discussion of Rubisco kinetics all numbering of k, $\Delta G^{\ddagger}$, $\Delta H^{\ddagger}$, $\Delta S^{\ddagger}$ refer to reaction steps initially described by Farquhar (1979) and reproduced in Figure 1. The Eyring equation has been previously used to calculate $\Delta G^{\ddagger}$ values for k_{catCO2}, k_{catO2}, and $S_{C/O}$ (Chen and Spreitzer, 1992; Tcherkez *et al.*, 2006; McNevin *et al.*, 2007; Tcherkez, 2013). Because k_{catCO2} and k_{catO2} are first order rate constants they have been represented as

$$-\ln\left(k_{catCO2}\frac{h}{k_B T}\right) RT = \Delta G^{\ddagger}_{kcatCO2} = \Delta H^{\ddagger}_{kcatCO2} - T\Delta S^{\ddagger}_{kcatCO2} \qquad \text{Eq. 9}$$

and

$$-\ln\left(k_{catO2}\frac{h}{k_B T}\right)RT = \Delta G^{\ddagger}_{kcatO2} = \Delta H^{\ddagger}_{kcatO2} - T\Delta S^{\ddagger}_{kcatO2}, \quad \text{Eq. 10}$$

and because $S_{C/O}$ is the ratio of two first order rate constants (Equation 6) it has been represented as

$$\ln\left(S_{C/O}\right)RT = \Delta G^{\ddagger}_{3} - \Delta G^{\ddagger}_{6} = (\Delta H^{\ddagger}_{3} - \Delta H^{\ddagger}_{6}) - T(\Delta S^{\ddagger}_{3} - \Delta S^{\ddagger}_{6}). \quad \text{Eq. 11}$$

The $\Delta G^{\ddagger}$ terms in Equations 9, 10, and 11 can be calculated directly from measured values, and the $\Delta H^{\ddagger}$ and $\Delta S^{\ddagger}$ terms would describe a linear fit to the temperature response, assuming $\Delta H^{\ddagger}$ and $\Delta S^{\ddagger}$ are constant within the temperature range. However, the use of Equations 9, 10, and 11 do not provide information regarding an elementary rate constant or a corresponding energy barrier. Further modeling to estimate individual rate constants from the measured data is described below.

Modeling of Radiolabel Data

Each of the rate constants (k) in Figure 1 has a corresponding energy of activation ($\Delta G^{\ddagger}$ from Equation 7), which has a corresponding enthalpic and entropic component ($\Delta H^{\ddagger}$ and $\Delta S^{\ddagger}$ from Equation 8). We assumed that the values of $\Delta H^{\ddagger}$ and $\Delta S^{\ddagger}$ are constant within the temperature range. Therefore, we fit Michaelis-Menten parameters calculated from elementary rate constants using Equations 2 through 6 to the measured Michaelis-Menten parameters by varying the corresponding $\Delta H^{\ddagger}$ and $\Delta S^{\ddagger}$ values. All modeling used the solver function in Excel (2016, Microsoft, Redmon, WA, USA) to minimize the sum of the differences squared between modeled and measured parameters.

The rate constants k_8 (cleavage of carboxylated intermediate) and k_9 (enolization of RuBP) were calculated from measured k_{catCO2} values following the calculations of Tcherkez *et al.* (2013) such that k_8/k_9 is 0.83 at 25 °C. The rate constant k_{10} (de-enolization) was modeled

assuming k_9/k_{10} is 0.43 at 25 °C following the calculations of Tcherkez *et al.* (2013), we further assumed that this ratio remained constant with temperature. This allowed for calculation of the rate of k_6 (CO_2 addition) as the only remaining unknown when fitting measured values of K_C with Equation 4 assuming k_7 (de-carboxylation) was negligible. After calculating k_6, k_3 (O_2 addition) was modeled from measured $S_{C/O}$ values and Equation 6, assuming rate constants k_7 (decarboxylation) and k_4 (deoxygenation) are negligible. Finally, the rate constant k_5 (cleavage of the oxygenated intermediate) was calculated from measured K_O values and Equation 7, again assuming k_4 (deoxygenation) was negligible. This process allowed for estimation of the temperature response for k and $\Delta G^{\ddagger}$ values for each step of the reaction mechanism listed in Equations 2 through 6, with the exception of the decarboxyalation and deoxygenation steps that were assumed negligible (Tcherkez *et al.*, 2013; Tcherkez, 2013; Tcherkez, 2016).

Modeling of MIMS Data

For the MIMS data, where measurements of k_{catO2} were available and non-linearity of Arrhenious plots were observed, the rate constants and corresponding $\Delta G^{\ddagger}$, $\Delta H^{\ddagger}$, and $\Delta S^{\ddagger}$ values were determined differently. The $\Delta H^{\ddagger}$ and $\Delta S^{\ddagger}$ values corresponding to the rate constants for k_8 (cleavage of carboxylated intermediate), k_5 (cleavage of oxygenated intermediate), and k_9 (RuBP enolization) were determined by fitting to measured k_{catCO2} and k_{catO2} values, assuming k_8/k_9 was 0.83 at 25 °C, and using Equations 2 and 3. Because k_{catCO2} showed a breakpoint, it is possible that k_8 and k_9 have different temperature responses, with a crossover at approximatly 25 °C. However, k_{catO2} also showed a breakpoint at 25 °C and the carbxylated intermediate cleavage rate (k_8) is much greater than the oxygenated cleavage rate (k_5) because measured k_{catCO2} values are greater than measured k_{catO2} . Therefore, a crossover of k_5, k_8, and k_9 at a single temperature is not

289 possible and a breakpoint in k_{catCO2} and k_{catO2} co-occuring at a single temperature cannot be
290 modeled as a changing rate limiting step. Therefore, we modeled the breakpoint in k_{catO2} by
291 allowing k_5 to have separate $\Delta H^{\ddagger}$ and $\Delta S^{\ddagger}$ values above and below the breakpoint, and assuming
292 k_9 had the same values of $\Delta H^{\ddagger}$ and $\Delta S^{\ddagger}$ above and below the breakpoint. Because k_9 (rate
293 constant of RuBP enolization) temperature response was assumed constant for models of k_{catO2}, it
294 was also assumed constant when modeling k_{catCO2}.Therefor, k_8 was allowed to have separate
295 values of $\Delta H^{\ddagger}$ and $\Delta S^{\ddagger}$ above and below the breakpoint. The k_{10} (rate constant of de-eneolization)
296 was subsequently calculated assuming the ratio k_9/k_{10} was 0.43 and constant with temperature.
297 The value k_6 (rate constant of CO_2 addition) was then calculated from measured K_C and the
298 approximation of Equation 4 assuming decarboxylation is negligible. This was also done for k_3
299 (rate constant for O_2 addition) using K_O and the approximation of Equation 5 assuming de-
300 oxygenation (k_4) was negligable. It was required that k_6 and k_3 have seperate $\Delta H^{\ddagger}$ and $\Delta S^{\ddagger}$ values
301 above and below the breakpoint to model linear Arrhenious plots of K_C and K_O. This process
302 provided estimates of the temperature response for k and $\Delta G^{\ddagger}$ values for each step of the reaction
303 mechanisms making up the measured Michaelis-Menten parameters (Equations 2 through 6),
304 with the exception of the decarboxyalation and deoxygenation steps, which were assumed
305 negligable.
306

307 RESULTS

308 **Breakpoints**

309 The Davies test indicated significant breakpoints for the k_{catCO2}, k_{catO2}, and $S_{C/O}$
310 temperature response for the MIMS data as well as for the Radiolabel single point measurement
311 of k_{catCO2} (Table 1, Figures 2 and 4). Both the Davies test and the maximum likelihood
312 segmented analysis indicated that the breakpoints in these parameters were near 25 °C (Table1).
313 All other parameters showed no breakpoints in their temperature responses for either the MIMS
314 or Radiolabel data sets (Table1, Figures 2, 3 and 4).

315

316 **Arrhenius Activation Energies and Modeled Value at 25 °C**

317 The E_a, and k_{25} for k_{catCO2}, k_{catO2} (Table 2), K_C, K_O, $S_{C/O}$ (Table 3) and ratios of interest
318 (Table 4) were calculated from the linear regressions shown in Figures 2 through 4. For the
319 MIMS derived parameters with breakpoints (k_{catCO2}, k_{catO2}, $S_{C/O}$), and the Radiolabel single point
320 estimate of k_{catCO2} the lower temperatures E_a values were larger than E_a values estimated at
321 higher temperatures (Table 2 and 3). Above 25 °C, the E_a values were similar for all parameters
322 between the Radiolabel and MIMS curve fitting methods. The Radiolabel E_a for k_{catCO2}
323 determined by curve fitting across all temperatures was intermediate to the two E_a values
324 estimated above and below the breakpoint from the single point Radiolabel data. The k_{25} values
325 for k_{catCO2} estimated from Radiolabel and MIMS methods were not different from each other, but
326 were larger than the k_{25} for k_{catO2} determined by MIMS (Table 2). The E_a and k_{25} values for K_C
327 and K_O were not significantly different between methods (Table 3). However, the MIMS $S_{C/O}$
328 measured from 10 to 25 °C had a lower (more negative) E_a value than the MIMS $S_{C/O}$ E_a value
329 measured from 25 to 40 °C and the Radiolabel $S_{C/O}$ E_a value (Table 3).

330 The E_a value for the carboxylation efficiency (k_{catCO2}/K_C) below 25 °C was significantly
331 different from zero for the MIMS method, where the carboxylation efficiency increased with
332 temperature; however, above 25 °C the E_a was not significantly different from zero (Table 4).
333 The MIMS E_a for oxygenation efficiency (k_{catO2}/K_O) was significantly different from zero above
334 and below 25 °C (Table 4). The E_a for the ratio of catalytic rates (k_{catCO2}/k_{catO2}) measured by
335 MIMS was only significantly different than zero above 25 °C (Table 4). The E_a for K_O/K_C was
336 significantly different from zero for both Radiolabel and MIMS methods (Table 4).
337
338 **Modeling *k* and $\Delta G^{\ddagger}$**
339 Above 25 °C the $\Delta G_3^{\ddagger}$-$\Delta G_6^{\ddagger}$ for $S_{C/O}$ from Radiolabel and MIMS (Fig. 5) are similar to
340 previous calculations for C_3 species reported by Tcherkez *et al.* (2006). However, the MIMS
341 entropy difference between O_2 and CO_2 addition ($\Delta S_3^{\ddagger}$-$\Delta S_6^{\ddagger}$, slope of line in Fig. 5, see Eq. 11,
342 Supp. Table 1), from data colleted below 25 °C appear more similar to the $\Delta S_3^{\ddagger}$-$\Delta S_6^{\ddagger}$ of red algae
343 rather than higher plants, when compared to data presented in Tcherkez *et al.* (2006).
344 The free energy of activation associated with k_{catCO2} ($\Delta G_{kcatCO2}^{\ddagger}$) plotted against
345 temperature, increased linearly for the Radiolabel curve fit method, while the $\Delta G_{kcatCO2}^{\ddagger}$
346 calculated from MIMS measurements decreased from 10 to 25 °C and then increased from 25 to
347 40 °C (Fig. 6). A similar temperature response was also observed for MIMS $\Delta G_{kcatO2}^{\ddagger}$, although
348 the absolute values of $\Delta G_{kcatO2}^{\ddagger}$ are larger than $\Delta G_{kcatCO2}^{\ddagger}$ as evident by a lower k_{catO2} compared
349 to k_{catCO2} at all temperatures (i.e. larger energy barriers result in slower reactions). The slope of
350 $\Delta G_{kcatCO2}^{\ddagger}$ values presented in Figure 6 (equivalent to the entropy term $\Delta S_{kcatCO2}^{\ddagger}$, Supp. Table 2)
351 calculated for Radiolabel and MIMS above 25 °C are slightly larger than those reported for

352 *Nicotiana tabacum* (McNevin *et al.*, 2007). The MIMS $\Delta S_{kcatCO2}^{\ddagger}$ and $\Delta S_{kcatO2}^{\ddagger}$ showed a sign
353 change above and below the breakpoint (negative slope to positive slope, Fig. 6, Supp. Table 2).
354 Temperature responses of the rate constants (k) and corresponding energy barriers of the
355 transition states ($\Delta G^{\ddagger}$) are shown in Figure 7, while the modeled $\Delta H^{\ddagger}$ and $\Delta S^{\ddagger}$ values are
356 presented in Suppemental Table 3. Calculations of elementary rate constants and corresponding
357 $\Delta G^{\ddagger}$ are similar to previous calculations at 25 °C from Tcherkez (2013) and Tcherkez (2016). In
358 order to model breakpoints in the MIMS k_{catCO2}, k_{catO2}, and $S_{C/O}$ parameters, breakpoints are
359 neeeded in the rate constants for the cleavage (k_8 and k_5) and for gas addition (k_6 and k_3). This is
360 required because it was not possible to model a simultaneous change in the rate limiting step for
361 both the k_{catCO2} and k_{catO2} parameter (Supp. Fig. 2). This further required that breakpoints were
362 needed in the rate constants for CO_2 and O_2 addition (k_6 and k_3, respectively) to maintain the
363 observed linearity for K_C and K_O Arrhenius plots (Fig. 2).
364

DISCUSSION

Temperature Responses of Rubisco Michaelis-Menten Kinetic Parameters

The Rubisco kinetic parameters for *Arabidopsis thaliana* measured with the Radiolabel and MIMS curve fitting methods were similar at and above 25 °C. Additionally, the modeled 25 °C values (k_{25}) and Arrhenius activation energy (E_a) above 25 °C agree with many of the literature values for other C_3-type Rubiscos, including *in vitro* and *in vivo* measurements of *A. thaliana* (Flexas *et al.*, 2007; Whitney *et al.*, 2011; Walker *et al.*, 2013; Weise *et al.*, 2015; Galmés *et al.*, 2016). Although, previous reports of Rubisco specificities for CO_2 over O_2 ($S_{C/O}$) at 25 °C vary widely for C_3 species, including for *A. thaliana* which range from below 2125 to above 2655 (Pa Pa^{-1}; Flexas *et al.*, 2007; Whitney *et al.*, 2011; Walker *et al.*, 2013; Weise *et al.*, 2015).

Galmés *et al.* (2016) highlighted contradictory trends in the temperature response of K_O when measured by *in vitro* assay; either increasing or decreasing with temperature (when expressed in units of molarity; converting between molarity and partial pressure changes the temperature response because the solubility of O_2 decreases with temperature). Here, both the Radiolabel and MIMS method show increases in K_O with temperature, with lower E_a values compared to K_C. The two data sets presented here confirm trends from the growing literature on C_3 Rubisco temperature responses, at least for values measured above 25 °C.

Alternatively, below 25 °C the Radiolabel and MIMS derived parameters had different temperature responses where the Arrhenius plots of MIMS determined k_{catCO2}, k_{catO2}, and $S_{C/O}$ were non-linear (Fig. 2, Fig. 4). Different temperature responses at high and low temperatures were interpreted as breakpoints for these kinetic parameters at 25 °C (Fig. 2). However, for the Radiolabel curve fit data all kinetic parameters appeared sufficiently linear. This could suggest

388 methodology artifacts; however, it is difficult to identify methodological errors that may give rise
389 to breakpoints given that they have also been observed by different laboratories using varying
390 methods and species (Badger and Collatz, 1977; Sage 2002, Kubien *et al.*, 2003; Sharwood *et*
391 *al.*, 2016).
392
393 **Evidence for Breakpoints in the Literature**
394 Björkman and Pearcy (1970) first identified a thermal breakpoint occurring in the
395 temperature response of V_{cmax} from two Atriplex species. However, in the same publication they
396 determined that the apparent breakpoints were caused by non-saturating or inhibitory bicarbonate
397 concentrations at varying temperatures and, when corrected, they obtained sufficiently linear
398 Arrhenius plots. Subsequently, Badger and Collatz (1977) identified breakpoints in k_{catCO2}, k_{catO2},
399 and K_C occuring at 15 °C, with sufficiently linear Arrhenius plots of K_O. While Badger and
400 Collatz (1977) did not discuss $S_{C/O}$, using Equation S6 with their data suggests a breakpoint in
401 $S_{C/O}$. Badger and Colloatz (1977) hypothesized that breakpoints were the result of possible
402 changes in enzyme conformation which change the rate limiting step of the reaction mechanism.
403 Sage (2002) idenified breakpoints in k_{catCO2} at 22 °C for *Oryza sativa*, but observed linear
404 Arrhenius plots for other species. Furthermore, Kubien *et al.* (2003) also observed a breakpoint
405 in k_{catCO2} between 12 and 18 °C for *Flaveria bidentis*, and suggested it was caused by
406 deactivation of the enzyme at low temperature, possibly by dissociation of the haloenzyme.
407 These analyses generally identified E_a values above the breakpoint similar to what is often
408 reported in the literature for the temperature response of Rubisco (E_a for k_{catCO2} ~60 kJ mol^{-1}),
409 with larger E_a values at low temperatures.

Recently, Sharwood *et al.* (2016) suggested breakpoints occuring at 25 °C for k_{catCO2} in eleven Panicoid grasses and tobacco. While E_a values at lower temperatures remain larger than the E_a values at higher temperatures, Sharwood *et al.*'s (2016) findings differs from the previous breakpoint publications, because the E_a below the breakpoint is around the expected value (~60 kJ mol^{-1}) and the E_a above the breakpoint is lower than expected (~30 kJ mol^{-1}). Sharwood *et al.* (2016) did not observe breakpoints in $S_{C/O,}$ but it is worth noting that they calculated $S_{C/O}$ from a separate assay from k_{catCO2} using the ratio of ^{3}H-glycerate to ^{3}H-glycolate as described here for the Radiolabel method. They also did not measure the temperature responses of K_C, K_O or k_{catO2} limiting direct comparisons to the data presented here.

Radiolabel Single Point k_{catCO2} Breakpoint

The Radiolabel single point method reported here utilized a single bicarbonate concentration with temperature (11 mM). This method resulted in a breakpoint, having an E_a value of 79.5 kJ mol^{-1} at low temperatures, and 42.1 kJ mol^{-1} at higher temperatures (Fig. 2, Table 2). Similar to Björkman and Pearcy (1970), the linear Arrhenius plot (Radiolabel curve fit) has an E_a value intermediate to the two E_a values determined when using a single bicarbonate concentration (~59.6 kJ mol^{-1}, Fig. 2, Table 2). Because Björkman and Pearcy (1970) suggested that there could be inhibition at low temperature and sub-saturating concentrations at high temperature, we plotted the predicted CO_2 concentration achieved by 11 mM $NaHCO_3$ at each temperature against the measured and modeled CO_2 response of the enzyme determined by both Radiolabel and MIMS curve fitting methods (Supp. Fig. 1). The CO_2 concentration provided by the 11 mM $NaHCO_3$ is less saturating at higher temperatures because the K_C of Rubisco

increases with temperature and the pK_a temperature response favors HCO_3^- at higher temperatures (Supp. Fig. 1).

From the data presented here, the CO_2 concentration appears saturating at 10 and 15 °C, but becomes increasingly less saturating at higher temperatures, as indicated where the shaded area intersects the modeled CO_2 response. This suggest the lower E_a value of the single point method at high temperatures could be caused by sub-saturating CO_2 concentrations. The sub-saturating CO_2 concentrations is likely due to both an increase in K_C with temperature and the predicted concentration of CO_2 decreases with temperature given the temperature response of the pK_a (Harned and Bonner, 1945). Alternatively, an inhibitory concentrations of CO_2 was not observed under any of the measurement conditions.

MIMS k_{catCO2}, k_{catO2}, and $S_{C/O}$ Breakpoints

The non-linearity of Arrhenius plots of k_{catCO2}, k_{catO2}, and $S_{C/O}$ for the MIMS data were interpreted as 25 °C breakpoints. Badger and Collatz (1977) also observed breakpoints in k_{catCO2}, k_{catO2}, and $S_{C/O;}$ however, they observed an additional thermal breakpoint in K_C, which was not observed with the MIMS data presented here. As $S_{C/O}$ is a ratio of k_{catCO2}, K_C, K_O, and k_{catO2} (Eq. S6), the differences in $S_{C/O}$ breakpoints between Badger and Collatz (1977) and our MIMS data could suggest different mechanisms driving the thermal response of $S_{C/O}$. Furthermore, no breakpoint in $S_{C/O}$ has been observed in any study using the ^{3}H-RuBP method.

The breakpoints observed in MIMS k_{catCO2} and k_{catO2} are unlikely to be caused by insufficient or inhibitory CO_2 concentrations, as is possible for the breakpoint observed in the Radiolabel single point k_{catCO2} measurement, as sub-saturation or inhibition should be evident in the CO_2 response curves (Supp. Fig. 1). A breakpoint in both k_{catCO2} and k_{catO2} could be caused

by deactivation of the enzyme as was suggested by Kubien *et al*. (2003). However, deactivation is unlikely to change the k_{catCO2}/k_{catO2} temperature response as was observed in Figure 3C, because both catalytic rates are expected to be affected in the same way by deactivation. Alternatively, the observed breakpoints in MIMS could be related to methodology as the Radiolabel Arrhenius plots presented here for k_{catCO2} and $S_{C/O}$ were sufficiently linear.

Nevertheless, breakpoints have persisted in the Rubisco literature for over forty years without sufficient explanation and warrant further investigations into their underlying causes. Badger and Collatz (1977) suggested changes in the rate-limiting step of the reaction mechanism brought about by conformational changes. If the elementary rate constants defining a specific parameter have different temperature responses then this could cause breakpoints if they crossover causing a change in rate limiting step. The discussion below utilizes the currently accepted reaction mechanism of Rubisco (Fig. 1) and transition state theory to explore breakpoints as a function of changes in energy barriers to elementary reactions.

Rubisco Reaction Mechanisms and Breakpoints

Radiolabel modelling

For the Radiolabel data, where all Arrhenius plots were sufficiently linear, a model of how the energy barriers for the Rubisco reaction mechanism change with temperature is presented in Figure 7, Panel C and E, and depicted as a kinetic energy barrier diagram in Panel A and B. As previously suggested by Tcherkez (2013) the k_{catCO2} and k_{catO2} values can be modeled assuming identical temperature responses for the rate of enolization (k_9), and cleavage for the carboxylated intermediate (k_8) and oxygenated-intermediate (k_5). Interestingly, the modeled addition of CO_2 ($\Delta G_6^{\ddagger}$) had high entropic cost leading to a decreasing temperature response for

the rate of CO_2 addition (k_6), suggesting the reaction becomes slower with increasing temperature. Additionally, the increase in the energy barrier for CO_2 addition ($\Delta G_6^{\ddagger}$) is greater than that for O_2 addition ($\Delta G_3^{\ddagger}$) such that the ratio k_6/k_3 decreased with temperature. This fits with the observation that $\Delta G_3^{\ddagger}$-$\Delta G_6^{\ddagger}$ decreases with temperature (Fig. 5). While our model for both CO_2 and O_2 addition has positive entropy of the transition states, the greater entropic cost for CO_2 addition could be the cause of $S_{C/O}$ decreases with temperature, more than would be assumed if $\Delta G_3^{\ddagger}$-$\Delta G_6^{\ddagger}$ remained constant with temperature.

MIMS modeling

For the MIMS data, the breakpoints observed in k_{catCO2} and k_{catO2} could be due to changes in rate limiting step as suggested by Badger and Collatz (1977). For example, k_{catCO2} is a function of the rate of cleavage of the carboxylated-intermediate (k_8) and the rate of RuBP enolization (k_9). This would mean that k_8 and k_9 have different temperature response such that they crossover around the breakpoint observed at 25 °C. However, modeling this change in rate limiting steps due to different temperature responses cannot simultaneously explain the observed breakpoint in k_{catCO2} and k_{catO2}, because the value of k_5 defining the cleavage of the oxygenated intermediate is lower than k_8. This means that k_9 cannot crossover both k_8 and k_5 at 25 °C (Supp. Fig. 2). Therefore, we proposed that rather than a crossover between elementary rate constants, a conformation change in the enzyme could change the temperature response for the cleavage reactions for both carboxylated (k_8) and oxygenated (k_5) intermediates (Fig. 7). The needed change in cleavage reactions (k_8 and k_5) to model a breakpoint suggests a positive entropy for the transition state below the breakpoint (decreasing $\Delta G_5^{\ddagger}$ with temperature) and a negative entropy of the transitions state above the breakpoint (increasing $\Delta G_5^{\ddagger}$ with temperature). While it seems

unlikely that such an entropy change could be driven by a conformation change in the enzyme brought about by such minimal changes in temperature, a similar change in entropy for k_{catCO2} was observed between wild type *Nicotiana tabacum* and a mutant (L335V) Rubisco (McNevin *et al.*, 2007). The amino acid substitution in the mutant was suggested to affect the loop that closes over RuBP as it is bound. This could suggest that the entropy changes to the cleavage reactions (k_5 and k_8) proposed here maybe possible given enzyme conformational changes with temperature.

The MIMS data also indicates a breakpoint in $S_{C/O}$ suggesting larger E_a values at low temperatures compared to higher temperatures, therefor the term $\Delta G_3^{\ddagger}$-$\Delta G_6^{\ddagger}$ was modeled with a non-linear temperature response (Fig. 5). As $S_{C/O}$ can be approximated as k_6/k_3, this could suggest a breakpoint in the temperature response of CO_2 addition (k_6), O_2 addition (k_3), or both. The individual values for k_6 and k_3 cannot be derived from $S_{C/O}$ measurements; however, in order for the observed constant temperature response of K_C and K_O to remain constant with temperature the cleavage reactions discussed above need to be offset by breakpoints in both k_6 and k_3 (Fig. 7F). Therefore, to model the reaction mechanism suggested by MIMS measurements, breakpoints in four elementary rate constants are needed to describe the breakpoints in k_{catCO2}, k_{catO2}, and $S_{C/O}$ but not in K_C or K_O.

The modeling presented here is largely based on isotope exchange studies, which suggest similar energy barriers between enolization ($\Delta G_9^{\ddagger}$) and cleavage ($\Delta G_8^{\ddagger}$). However, these measurements have been limited to 25 °C (Van Dyk and Schloss, 1986; Tcherkez *et al.*, 2013) and extension of isotope exchange studies to temperature responses would help constrain how the elementary rate constants vary with temperature. Contrary to the above proposal that the cleavage transition state (k_8) undergoes changes above and below 25 °C, is that Rubisco

524 discrimination against $^{13}CO_2$ is believed to remain constant with temperature (Christeller *et al.*,
525 1976). If the rate of cleavage (k_8) decreases, then the decarboxylation reaction (k_7) may increase,
526 or the ratio k_7/k_8 could increase, which would change Rubisco discrimination against $^{13}CO_2$.
527 Furthermore, the above modeling relies on the assumption that decarboxylation (k_7) was
528 negligible at all temperatures; therefore, changes in fractionation with temperature for an enzyme
529 exhibiting breakpoints should help test the validity of these assumptions.
530
531 CONCLUSION
532 The measured temperature responses of Rubisco kinetic parameters were consistent
533 between methods at and above 25 °C; however, there were thermal breakpoints at ~ 25 °C in the
534 MIMS dataset for k_{catCO2}, k_{catO2}, and $S_{C/O}$. Additionally, the Radiolabel method using a single
535 bicarbonate concentration showed a breakpoint for k_{catCO2} at 25 °C but the curve fitting did not,
536 suggesting this breakpoint was caused in part by non-saturating CO_2 concentrations at higher
537 temperatures. Previous studies suggest that breakpoints are caused by either a change in the rate
538 limiting step of the reaction mechanism or deactivation of the enzyme at low temperatures. By
539 modeling elementary steps of the reaction mechanism, we showed that a simple change in rate
540 limiting step is not sufficient to explain simultaneous breakpoints in both k_{catCO2} and k_{catO2}, and
541 that breakpoints in the elementary rate constants are likely needed. Additionally, it is unclear
542 how deactivation would cause the observed breakpoint in $S_{C/O}$. Moving forward, the temperature
543 response of isotopic substitutions experiments would advance our understanding of how
544 elementary rate constants change in relation to one another with temperature.
545
546

ACKNOWLEDGEMENT

This work was supported by the Division of Chemical Sciences, Geosciences, and Biosciences, Office of Basic Energy Sciences, Department of Energy (grant no. DE–FG02–09ER16062), the National Science Foundation (Major Research Instrumentation grant no. 0923562), the National Science and Engineering Research Council of Canada (Discovery grant no. 327103; and PGS-D scholarship to APC), and the Seattle chapter of the Achievement Rewards for College Scientists Foundation (R.A.B.). A.B.C. and D.S.K. proposed the original concept and design for the project; R.A.B. and A.P.C. performed the experiments and data analysis; R.A.B. wrote the article with the contributions of all the authors; A.B.C. supervised and complemented the writing. We would like to thank Chuck Cody for maintaining plant growth facilities and current members of Cousins Lab for helpful and insightful discussions.

559 LITERATURE CITED

560 Andrews T.J., Lorimer G.H., Tolbert N.E. (1973) Ribulose diphosphate oxygenase. I. Synthesis
561 of phosphoglycolate by fraction-1 protein of leaves. *Biochemistry* 12(1), 11-18.
562
563 Badger M.R. and Collatz G.J. (1977) Studies on the kinetic mechanism of ribulose-1, 5-
564 bisphosphate carboxylase and oxygenase reactions, with particular reference to the effect of
565 temperature on kinetic parameters. *Carnegie Institute of Washington, Yearbook* 76, 355-361.
566
567 Björkman O. and Pearcy R.W. (1970) Effect of growth temperature on the temperature
568 dependence of photosynthesis in vivo and on CO_2 fixation by carboxydismutase *in vitro* in C_3
569 and C_4 species. *Carnegie Institution of Washington, Yearbook* 70, 511-520.
570
571 Bowes G., Ogren W.L., Hageman R.H. (1971) Phosphoglycolate production catalyzed by
572 ribulose diphosphate carboxylase. *Biochemical and Biophysical Research Communications*
573 45(3), 716-722.
574
575 Boyd R.A., Gandin A., Cousins A.B. (2015) Temperature Responses of C_4 Photosynthesis:
576 Biochemical Analysis of Rubisco, Phosphoenolpyruvate Carboxylase, and Carbonic Anhydrase
577 in *Setaria viridis*. *Plant Physiology* 169, 1850-1861.
578
579 Chen Z. and Spreitzer R. J. (1992) How various factors influence the CO_2/O_2 specificity of
580 Ribulose-1, 5-bisphosphate carboxylase/oxygenase. *Photosynthesis Research* 31(2), 157-164.
581

582 Christeller J.T., Laing W.A., Troughton J.H. (1976) Isotope Discrimination by Ribulose 1,5-
583 Diphosphate Carboxylase. *Plant Physiology* 57(4), 580-582.
584
585 Cousins A.B., Ghannoum O., von Caemmerer S., Badger M.R. (2010) Simultaneous
586 determination of Rubisco carboxylase and oxygenase kinetic parameters in *Triticum aestivum*
587 and *Zea mays* using membrane inlet mass spectrometry. *Plant, Cell & Environment* 33, 444-452.
588
589 Crafts-Brander S.J. and Salvucci M.E. (2000) Rubisco activase constrains the photosynthetic
590 potential of leaves at high temperature and CO_2. *Proceedings of the National Academy of*
591 *Sciences of the United States of America* 97(24), 13430-13435.
592
593 Davies R.B. (1987) Hypothesis testing when a nuisance parameter is present only under the
594 alternatives. *Biometrika* 74(1), 33-43.
595
596 Edsall J.T., Wyman J. (1958) Carbon dioxide and carbonic acid. In: *Biophysical Chemistry* (eds.
597 J.T. Edsall, J. Wyman), pp 550-590. Academic Press, New York, London.
598
599 Farquhar G.D. (1979) Models describing the kinetics of ribulose biphosphate carboxylase-
600 oxygenase. *Archives of Biochemistry and Biophysics*, 193(2), 456-468.
601
602 Flexas J., Ortuño M., Ribas-Carbo M., Diaz-Espejo A., Flórez-Sarasa I., Medrano H. (2007)
603 Mesophyll conductance to CO_2 in *Arabidopsis thaliana*. *New Phytologist* 175, 501-511.
604

605 Galmés J., Hermida-Carrera C., Laanisto L., Niinemets U. (2016) A compendium of temperature
606 responses of Rubisco kinetic traits: variability among and within photosynthetic groups and
607 impacts on photosynthesis modeling. *Journal of Experimental Botany* 67(17), 5067-5091.
608
609 Harned H.S. and Bonner F.T. (1945) The first ionization of carbonic acid in aqueous solutions of
610 sodium chloride. *Journal of the American Chemical Society* 67, 1026-1031.
611
612 Hurwitz J., Jakoby W.B., Horecker B.L. (1956) On the mechanism of CO_2 fixation leading to
613 phosphoglyceric acid. *Biochimica et Biophysica Acta* 22(1), 194-195.
614
615 Jordan D.B. and Ogren W.L. (1981) A sensitive assay procedure for simultaneous determination
616 of ribulose-1, 5-bisphosphate carboxylase and oxygenase activities. *Plant Physiology* 67(2), 237-
617 245.
618
619 Kane H.J., Viil J., Entsch B., Paul K., Morell M.K., Andrews T.J. (1994) An improved method
620 for measuring the CO_2/O_2 specificity of ribulose-bisphosphate carboxylase-oxygenase.
621 *Australian Journal of Plant Physiology* 21, 449-461.
622
623 Kubien D.S., Brown C.M., Kane H.J. (2011) Quantifying the amount and activity of rubisco in
624 leaves. In: *Methods in Molecular Biology, Photosynthesis Research Protocols* (ed. R.
625 Carpentier), pp 349-362. Humana Press, New York.
626

627 Kubien D.S., von Caemmerer S., Furbank R.T., and Sage, R.F. (2003) C_4 photosynthesis at low
628 temperature. A study using transgenic plants with reduced amounts of Rubisco. *Plant Physiology*
629 132(3), 1577-1585.
630
631 Kubien D.S., Whitney S.M., Moore P.V., Jesson L.K. (2008) The biochemistry of Rubisco in
632 Flaveria. *Journal of Experimental Botany* 59, 1767-1777.
633
634 McNevin D.B., Badger M.R., Kane H.J., Farquhar G.D. (2006) Measurement of (carbon) kinetic
635 isotope effect by Rayleigh fractionation using membrane inlet mass spectrometry for CO_2-
636 consuming reactions. *Functional Plant Biology* 33(12), 1115-1128.
637
638 McNevin D.B., Badger M.R., Whitney S.M., von Caemmerer S., Tcherkez G.G., Farquhar, G.D.
639 (2007) Differences in carbon isotope discrimination of three variants of d-ribulose-1, 5-
640 bisphosphate carboxylase/oxygenase reflect differences in their catalytic mechanisms. *Journal of*
641 *Biological Chemistry* 282(49), 36068-36076.
642
643 Muggeo V.M. (2003) Estimating regression models with unknown break‐points. *Statistics in*
644 *Medicine* 22(19), 3055-3071.
645
646 Muggeo V.M. (2008) Segmented: An R package to fit regression models with broken-line
647 relationships. *R news* 8(1), 20-25.
648

O'Leary M.H., Madhavan S., Paneth P. (1992) Physical and chemical basis of carbon isotope fractionation in plants. *Plant, Cell & Environment* 15(9), 1099-1104.

Paul K., Morell M.K., Andrews T.J. (1991) Mutations in the small subunit of ribulose bisphosphate carboxylase affect subunit binding and catalysis. *Biochemistry* 30, 10019-10026.

Perdomo J.A., Cavanagh A.P., Kubien D.S., Galmés J. (2015) Temperature dependence of *in vitro* Rubisco kinetics in species of Flaveria with different photosynthetic mechanisms. *Photosynthesis Research* 124, 67-75.

Pittermann J. and Sage R.F. (2000) Photosynthetic performance at low temperature of Bouteloua gracilis Lag., a high-altitude C_4 grass from the Rocky Mountains, USA. *Plant, Cell & Environment* 23(8), 811-823.

Ruuska S., Andrews T.J., Badger M.R., Hudson G.S., Laisk A., Price G.D., von Caemmerer S. (1998) The interplay between limiting processes in C-3 photosynthesis studied by rapid-response gas exchange using transgenic tobacco impaired in photosynthesis. *Australian Journal of Plant Physiology* 25, 859-870.

Sage R.F. (2002) Variation in the k_{cat} of Rubisco in C_3 and C_4 plants and some implications for photosynthetic performance at high and low temperature. *Journal of Experimental Botany* 53, 609-620.

672 Sage R.F., Santrucek J., Grise D.J. (1995) Temperature effects on the photosynthetic response of
673 C3 plants to long-term CO2 enrichment. *Vegetatio* 121, 67-77.
674
675 Sander R. (2015) Compilation of Henry's law constants (version 4.0) for water as solvent.
676 *Atmospheric Chemistry and Physics* 15, 4399-4981.
677
678 Sharwood R.E., Ghannoum O., Kapralov M.V., Gunn L.H., Whitney S.M. (2016) Temperature
679 responses of Rubisco from Paniceae grasses provide opportunities for improving C_3
680 photosynthesis. *Nature Plants* 2, 16186.
681
682 Shay P.E., Kubien D.S. (2013) Field analysis of photoprotection in co‐occurring cool climate
683 C_3 and C_4 grasses. *Physiologia Plantarum* 147(3), 316-328.
684
685 Spreitzer R.J., Salvucci M.E. (2002) Rubisco: structure, regulatory interactions, and possibilities
686 for a better enzyme. *Annual Review of Plant Biology* 53(1), 449-475.
687
688 Tcherkez G. (2013) Modelling the reaction mechanism of ribulose-1, 5-bisphosphate
689 carboxylase/oxygenase and consequences for kinetic parameters. *Plant, Cell & Environment*
690 36(9), 1586-1596.
691
692 Tcherkez G. (2016) The mechanism of Rubisco-catalysed oxygenation. *Plant, Cell &*
693 *Environment* 39(5), 983-997.
694

Tcherkez G.G., Bathellier C., Stuart-Williams H., Whitney S., Gout E., Bligny R., Farquhar G.D. (2013) D_2O solvent isotope effects suggest uniform energy barriers in ribulose-1, 5-bisphosphate carboxylase/oxygenase catalysis. *Biochemistry* 52(5), 869-877.

Tcherkez G.G., Farquhar G.D., Andrews T.J. (2006) Despite slow catalysis and confused substrate specificity, all ribulose bisphosphate carboxylases may be nearly perfectly optimized. *Proceedings of the National Academy of Sciences* 103(19), 7246-7251.

Tieszen L. and Sigurdson D. (1973) Effect of temperature on carboxylase activity and stability in some Calvin cycle grasses from the arctic. *Arctic, Antarctic, and Alpine Research* 5(1), 59-66.

Ubierna N., Gandin A., Boyd R.A., Cousins A.B. (2017) Temperature response of mesophyll conductance in three C_4 species calculated with two methods: ^{18}O discrimination and *in vitro* V_{pmax}. *New Phytologist* 214(1), 66-80.

Van Dyk D.E. and Schloss J.V. (1986) Deuterium isotope effects in the carboxylase reaction of ribulose-1, 5-bisphosphate carboxylase/oxygenase. *Biochemistry*, 25(18), 5145-5156.

von Caemmerer S. (2000) *Biochemical models of leaf photosynthesis*. Csiro Publishing, Collingwood, Australia

716 Walker B., Ariza L.S., Kaines S., Badger M.R., Cousins A.B. (2013) Temperature response of *in*
717 *vivo* Rubisco kinetics and mesophyll conductance in *Arabidopsis thaliana*: comparisons to
718 *Nicotiana tabacum*. *Plant, Cell & Environment* 36, 2108-2119.
719
720 Weise S.E., Carr D.J., Bourke A.M., Hanson D.T., Swarthout D., Sharkey T.D. (2015) The *arc*
721 mutants of *Arabidopsis* with fewer large chloroplasts have a lower mesophyll conductance.
722 *Photosynthesis Research* 124(1), 117-126.
723
724 Whitney S.M., Houtz R.L., Alonso H. (2011) Advancing our understanding and capacity to
725 engineer nature's CO_2-sequestering enzyme, Rubisco. *Plant Physiology* 155(1), 27-35.
726
727

Table 1. Testing for thermal breaks for all kinetic parameters. Arrhenius plots were examined using the package 'segmented' in R (R Core Team, 2013, http://www.R-project.org/), which determines significance of breakpoints in linear models and estimates breakpoint locations as described by Davies (1987). Additionally, breakpoint locations and confidence intervals (CI, lower and upper) were independently estimated using a maximum likelihood test (Muggeo 2003; Muggeo 2008). Where * indicates a p-value < 0.05 for the Davies test and ns = not significant.

Method	**Parameter**	**Davies Test**		***Maximum likelihood***		
		Estimated Breakpoint (°C)	p-value	Estimated Breakpoint (°C	*CI* (lower)	CI (upper)
Radiolabel						
	k_{catCO2} single point	26.8	*	25.1	5.3	36.9
	k_{catCO2} curve fit	-	ns			
	k_{catO2}	-	-			
	K_C	-	ns			
	K_O	-	ns			
	$S_{C/O}$	-	ns			
MIMS						
	k_{catCO2}	25.3	*	25.3	23.1	31.5
	k_{catO2}	25.3	*	25.5	24.3	32.6
	K_C	-	ns			
	K_O	-	ns			
	$S_{C/O}$	25.4	*	25.2	15.0	27.6

728

729

Table 2. Comparison of k_{25} and E_a values for k_{cat} measurements from the different methods. The k_{25} and E_a values are the mean of three to four replicates, calculated from linear regressions of Arrhenius plots. The temperature ranges for each regression were determined by segment analysis. Superscripts indicate significant differences between groups (Tukey HSD, $p < 0.05$).

Method	**Temperature (°C)**	**Parameter**	k_{25}		E_a	
Radiolabel						
single point	0 - 25	k_{catCO2} (s^{-1})	3.50	$\pm 0.20^{A}$	79.53	$\pm 2.03^{a}$
	25 - 40		--	--	42.11	$\pm 3.45^{c}$
curve fit	10 - 35		3.10	$\pm 0.07^{A}$	59.64	$\pm 3.93^{b}$
MIMS	10 - 25		3.53	$\pm 0.25^{A}$	90.36	$\pm 1.03^{a}$
	25 - 40		--	--	62.20	$\pm 2.68^{b}$
	10 - 25	k_{catO2} (s^{-1})	1.38	$\pm 0.05^{B}$	92.95	$\pm 7.31^{a}$
	25 - 40		--	--	47.11	$\pm 2.33^{bc}$

Table 3. Comparison of K_C, K_O, $S_{C/O}$ parameters k_{25} and E_a resulting from the different methods are shown. No differences were observed in k_{25} between methods. No differences were observed in E_a values for K_C and K_O values between methods (ANOVA). The superscripts next to the E_a values indicate significant differences for the $S_{C/O}$ values (Tukey HSD, $p < 0.05$).

Method	**Temperature Range (°C)**	**Parameter**	**k_{25} (Pa)**		**E_a (kJ mol^{-1})**	
Radiolabel	10 - 35	K_C	36	±2	63.09	±6.23
MIMS	10 - 40		34	±1	62.62	±3.44
Radiolabel	15 - 35	K_O	23100	±3430	16.89	±2.59
MIMS	10 - 40		24400	±701	17.01	±2.48
Radiolabel	5 - 40	$S_{C/O}$	2003	±22	-28.66	±0.51[b]
MIMS	10 - 25		1814	±117	-48.19	±4.17[a]
	25 - 40		--	--	-30.51	±6.41[b]

Table 4. The E_a and k_{25} parameters for k_{catCO2}/K_C, k_{catO2}/K_O, k_{catCO2}/k_{catO2}, and K_O/K_C ratios. The E_a parameters were tested to determine if they were significantly different than zero (t-test), where the * next to the E_a values indicates a p-value below 0.05.

Method	**Temperature Range (°C)**	**Parameter**	k_{25}		E_a	
Radiolabel	10 - 35	k_{catCO2}/K_C	0.09	±0.00	-3.45	±3.94
MIMS	10 - 25	(s^{-1} Pa^{-1})	0.10	±0.01	27.75	±3.38*
	25 - 40		--	--	-0.41	±6.10
MIMS	10 - 25	k_{catO2}/K_O	0.06	±0.00	75.93	±7.41*
	25 - 40	(s^{-1} kPa^{-1})	--	--	30.09	±0.70*
MIMS	10 - 25	k_{catCO2}/k_{catO2}	2.55	±0.16	-2.58	±6.73
	25 - 40		--	--	15.10	±4.92*
Radiolabel	15 - 35	K_O/K_C	0.65	±0.11	-46.20	±8.80*
MIMS	10 - 40	(kPa Pa^{-1})	0.71	±0.01	-45.60	±2.57*

741

742

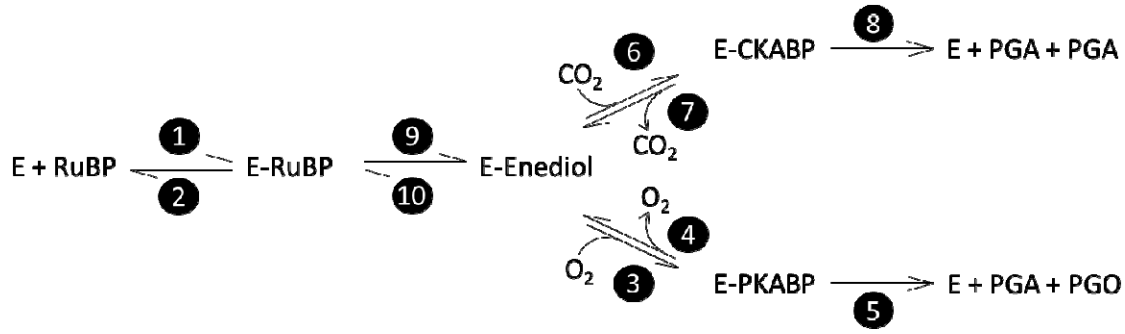

Figure 1. Elementary reactions of Rubisco-catalyzed carboxylation and oxygenation reproduced from Farquhar (1979). Each reaction, forward and reverse, is numbered in a filled circle following the numbering from Farquhar (1979). Steps 8 and 5 are written as irreversible reactions. Step 8 includes cleavage, hydration, and reprotonation as a single step. Step 5 includes cleavage and hydration as a single step. Each step is associated with a rate constant (k) and energy of activation ($\Delta G^{\ddagger}$) following the same numbering as shown in filled circles. Abbreviations as follows: E, free activated enzyme; RuBP, D-ribulose-1,5-bisphosphate; E-RuBP; enzyme bound RuBP; E-Enediol, enzyme bound 2,3-enediolate form of RuBP; CO_2, carbon dioxide; E-CKABP, enzyme bound carboxyketone intermediate; PGA, 3-phospho-D-glycerate; O_2, oxygen; E-PKABP, peroxo intermediate; PGO, 2-phospho-glycolate.

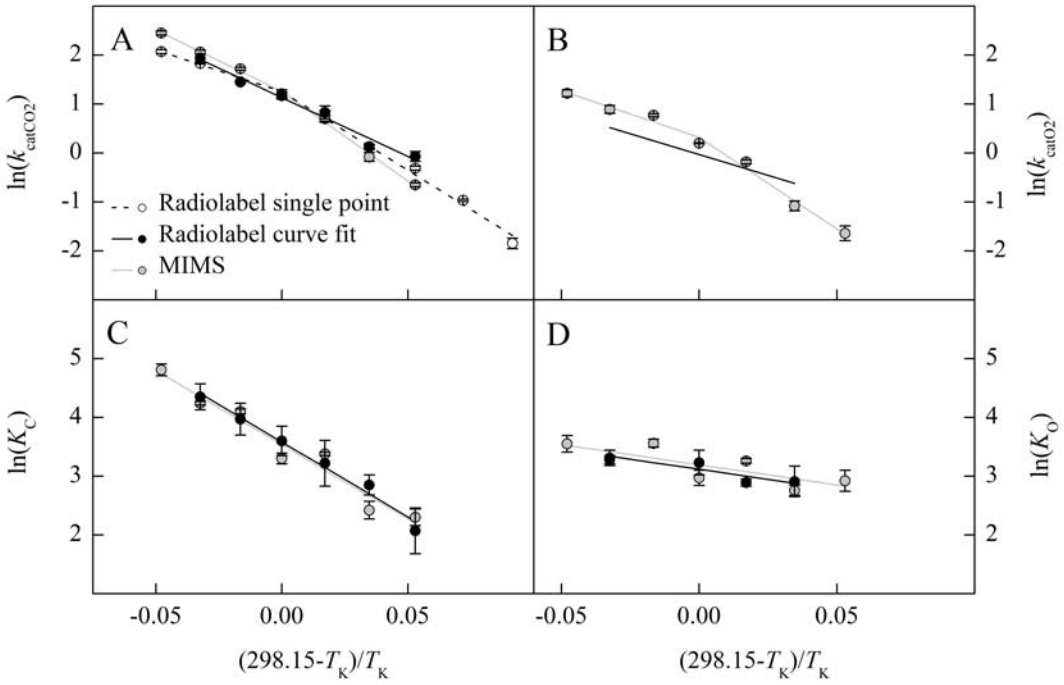

Figure 2. The natural log of Rubisco parameters from *Arabidopsis thaliana* measured using Radiolabel (single point, open circle; curve fit, black circle) and MIMS (grey circle) methods are plotted against the inverse of the temperature in Kelvin offset to a y-intercept of 25 °C. The temperature response of catalytic turnover for CO_2 (k_{catCO2}, s^{-1}, Panel A), and O_2 (k_{catO2}, s^{-1}, Panel B), the Michaelis-Menten constant for CO_2 (K_C, Pa, Panel C), and O_2 (K_O, kPa, Panel D) are shown. The lines represent the model fit to the measured data. The Radiolabel k_{catO2} model in panel B was determined from the relationship with $S_{C/O}$ described by Equation S6.

766

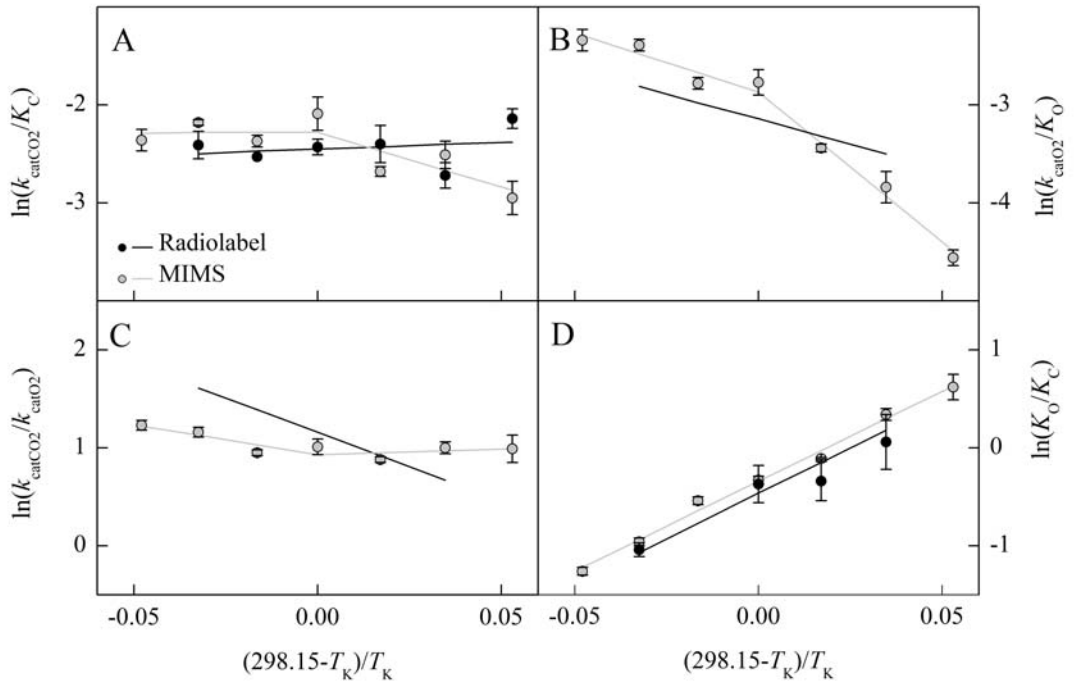

767

768 **Figure 3.** The natural log of the Rubisco parameter ratios from *Arabidopsis thaliana* measured
769 using Radiolabel (black circle) and MIMS (grey circle) are plotted against the inverse of the
770 temperature in Kelvin offset to a y-intercept of 25 °C. The temperature response of the catalytic
771 efficiency of the carboxylation (k_{catCO2}/K_C, Panel A) and oxygenation (k_{catO2}/K_O, Panel B)
772 reactions, catalytic turnover ratio for CO_2 over O_2 (k_{catCO2}/k_{catO2}, Panel C), and the Michaelis-
773 Menten constant ratio for O_2 over CO_2 (K_O/K_C, Panel D) are shown. Lines represent the
774 combination of models represented in Figure 2 and are not the result of linear regressions to the
775 ratios.

776

777

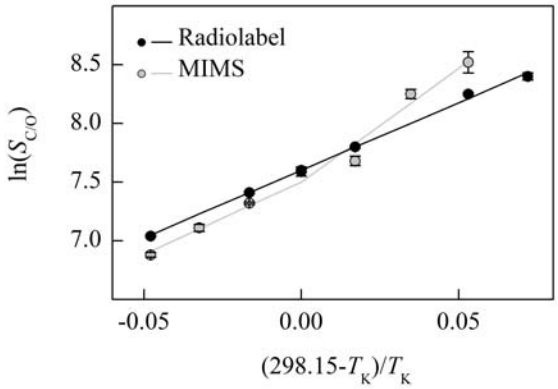

778

779 **Figure 4.** The natural log of Rubisco specificity for CO_2 over O_2 ($S_{C/O}$) from *Arabidopsis*
780 *thaliana* measured using Radiolabel (black circle) and MIMS (grey circle) methods are plotted
781 against the inverse of the temperature in Kelvin offset to a y-intercept of 25 °C. The black line
782 represents the model fit to the measured Radiolabel values. The grey line was determined from
783 the relationship of $S_{C/O}$ to the parameters presented in Figure 2, described by Equation S6.

784

785

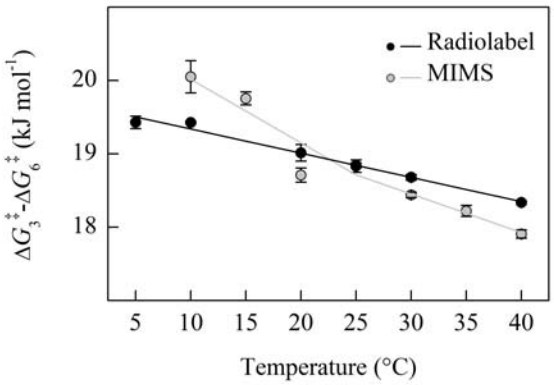

786

787 **Figure 5.** The temperature response of $\Delta G_3^{\ddagger}$-$\Delta G_6^{\ddagger}$ calculated from the data presented in Figure 4.

788 Both measurement methods show a decrease with temperature. Solid black circles are the mean

789 of four replicates measured using Radiolabel, filled grey circles are the means from three

790 replicates using MIMS, standard error is shown. The solid lines indicate the linear regression fit

791 to calculated values.

792

793

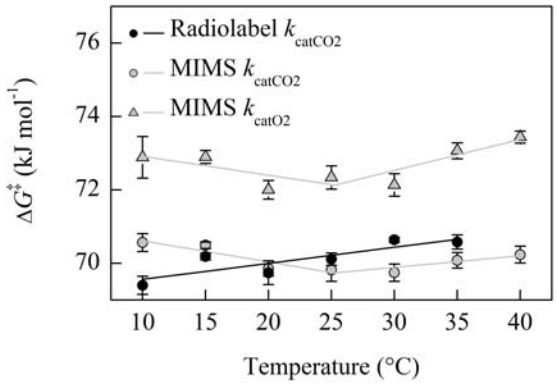

Figure 6. The temperature response of $\Delta G_{kcatCO2}^{\ddagger}$ for MIMS and Radiolabel methods, and $\Delta G_{kcatO2}^{\ddagger}$ for MIMS calculated from the data presented in Figure 2. Two regressions were fit to the MIMS data on either side of the 25 °C breakpoint, a single regression is fit to the Radiolabel data. Solid black circles are the mean of three replicates measured using Radiolabel, filled grey circles are the means from three replicates using MIMS, standard error is shown.

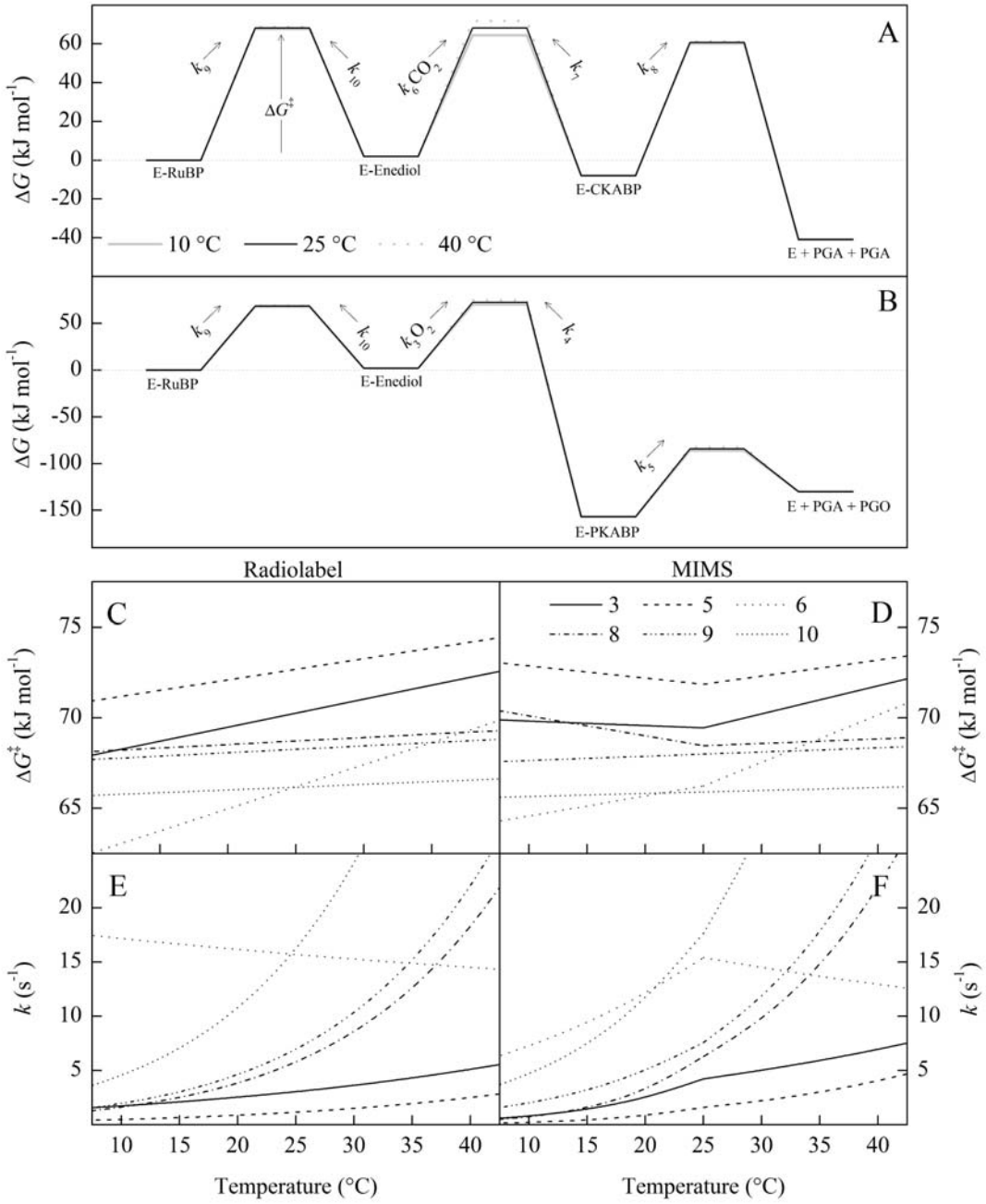

Figure 7. A kinetic energy barrier diagram showing the modeled temperature responses of the energy barrier to the transition state ($\Delta G^{\ddagger}$) and the corresponding first order rate constant *k*. The $\Delta G^{\ddagger}$ and *k* are indicated by the numbered step of the reaction following Figure 1. The assumptions made for this model are stated in the methods section. For steps 3 and 6 (O_2 and

809 CO_2 addition, respectively), the rate constants were multiplied by ambient concentrations O_2 (21
810 kPa) and CO_2 (41 Pa) as a pseudo-first order approximation for comparison to the other rate
811 constants and to calculate their respective $\Delta G^{\ddagger}$. For the bottom figure, the left-hand column is
812 modeled on the Radiolabel data and the right-hand column on the MIMS data so that
813 comparisons between continuous and breakpoint temperature responses can be made. The values
814 for intermediates were taken from Tcherkez (2013) for Panel A and Tcherkez (2016) for Panel B
815 and assumed to remain constant with temperature.
816